JOURNAL OF AIRCRAFT
Vol. 37, No. 3, May–June 2000

High Reynolds Number, Multielement Airfoil Flowfield Measurements

Frank W. Spaid*
The Boeing Company, St. Louis, Missouri 63166

A unique set of high Reynolds number experimental results are presented that illustrate some of the crucial flow physics issues controlling the aerodynamic performance characteristics of transport-aircraft-type high-lift geometries. Data include static-pressure distributions, lift and drag measurements, and boundary-layer and wake surveys. Results presented provide important insights into the underlying causes of differences in performance associated with various geometry modifications. The two most significant and instructive examples involve the effects of a relatively small flap gap change at a fixed flap deflection and the effects of an increase in flap deflection. For the former, decreasing the flap gap eliminates an observed flow separation on the flap at (lower) approach angles of attack, but also results in a reduction in maximum lift caused by enhanced merging and spreading of the wakes above the flap. For the latter, it is observed that the wake spreading is increased substantially at the higher flap deflection, thereby minimizing improvement in maximum lift. These data have been used for computational fluid dynamics (CFD) code calibration and should provide a means to identify the shortcomings of existing CFD methods, thereby identifying areas where improvements are required.

Nomenclature

C_f = skin-friction coefficient, τ_w / q_∞
C_l = lift coefficient
C_p = pressure coefficient, $(p - p_\infty)/q_\infty$
C_{pt} = local total pressure in coefficient form
q = dynamic pressure, $\frac{1}{2}(\rho U^2)$
U = velocity magnitude
x/c = reference axial location of traverse on model surface normalized by clean airfoil chord, measured from nose of clean airfoil; value refers to the airfoil in the clean configuration
y/c = distance normal to the local surface, normalized by the chord
α = angle of attack
δ = uncertainty in quantites derived from five-hole probe measurements
δ^* = displacement thickness
θ = pitch-plane flow inclination relative to local model surface, positive upward
ρ = density

Subscript

∞ = freestream, tunnel reference

Introduction

CURRENT design methods or computational fluid dynamics (CFD) methods are presently incapable of predicting the performance of multielement configurations to the level of accuracy that is necessary for high-lift system design. Accurate modeling of the very complex flowfields associated with high-lift configurations, including confluent boundary layers and merging wakes from multiple elements, is essential to predict the performance of such configurations. Detailed flowfield measurements are necessary to improve our understanding of the fluid physics governing performance of high-lift systems from which improved designs can be derived and to provide a basis for improvements in CFD codes tailored to the design and analysis of high-lift systems.

Reynolds number variations have been shown to have a large impact on the performance of high-lift configurations, and observed variations in key performance parameters with variations in Reynolds number do not follow trends that allow reliable extrapolation.[1,2] Therefore, it is important to make flowfield measurements at Reynolds numbers representative of flight conditions. Studies reporting measurements obtained in flows about multielement airfoils have been published previously[3,4]; however, these results typically correspond to either idealized configurations or have been made at Reynolds numbers too low to be of direct practical value.

The experimental data presented here were obtained with a representative multielement airfoil at Reynolds numbers approaching flight conditions and include angles of attack up to and beyond maximum lift. This project utilized a unique traversing unit that is sufficiently rigid to withstand the high dynamic and unsteady pressures associated with high Reynolds number operation, but is also sufficiently slender to cause acceptably small flowfield interference. This paper summarizes results presented in Refs. 5 and 6, with emphasis on the most important results from surface static-pressure measurements and flowfield surveys with five-hole and flat-tube probes. The present work has been extended by Bertelrud[7] using arrays of surface hot-film anemometers and by McGinley et al.[8] using hot-wire anemometry. Comparisons of the data with results of CFD simulations are presented in Refs. 9 and 10.

Experimental Methods

Test Facility and Model Description

Testing was performed at the NASA Langley Low Turbulence Pressure Tunnel (LTPT). The LTPT is a closed-throat, single-return wind tunnel that can be pressurized up to 10 atm. Reynolds numbers approaching full-scale flight conditions can be obtained in tests of nominally two-dimensional airfoil models at low Mach numbers in this facility. Although the investigation included data obtained at several values of Reynolds number, all of the data presented in this summary were obtained at a Reynolds number based on airfoil chord in the clean configuration of 9×10^6. The test section of the tunnel is 3.0 ft wide and 7.5 ft high. Airfoil models are supported by turntables in the sidewalls connected to an inner drum assembly of an external balance. Models can be pitched about the midchord point of the stowed airfoil through a range of -4 to 24 deg.

Presented as Paper 96-0682 at the 34th Aerospace Sciences Meeting and Exhibit, Reno, NV, 15–19 January 1996; received 8 April 1999; revision received 10 December 1999; accepted for publication 18 December 1999.

*Manager, Experimental Fluid Dynamics, Retired. Associate Fellow AIAA.

A boundary-layer control system is used to promote two-dimensional flow by reducing tunnel sidewall boundary-layer effects. The system utilizes the pressure difference between the tunnel and atmosphere to apply suction to the sidewall boundary layers near the model through porous plates. The suction is controlled by setting valves at the onset of each run to obtain nearly uniform spanwise pressures at a high angle of attack. Studies have been performed to determine the optimal porous area pattern.

A wake-rake traverse system is used to measure drag, consisting of three five-hole probes connected to an arm that traverses vertically in the center (midspan) of the tunnel aft of the model.

The model is a three-element, high-lift configuration model that spans the test section and has a clean (stowed) airfoil chord of 22 in. The model is a 11.55% thick airfoil; the chords of the slat and flap are 14.48 and 30%, respectively. Four rows of streamlined support brackets for each of the high-lift devices were required because of the high loads developed at maximum lift conditions. Chordwise pressure-tap rows are located at 50 and 77% span. Spanwise rows of pressure taps are located at the trailing edge of each element and on the flap upper surface.

Data were obtained for four multielement configurations. Figure 1 illustrates rigging terminology for multielement airfoils, and the slat and flap settings are presented in Tables 1 and 2. Figure 2 shows a cross-sectional view of the baseline configuration (configuration A) with locations of typical flow survey stations and also presents overlays of the alternate configurations for comparison with the baseline. The flow survey stations are identified as fractions of the clean airfoil chord. Figure 2c shows that configuration C is primarily a change in flap deflection relative to configuration A. However, Table 2 shows that configuration C is also associated with small changes in gap and overhang relative to configuration A.

Table 1 Slat gap and overhang positions (% of chord)

Configuration	Gap	Overhang
A, B, C, D	2.91	−2.50
	2.48	−2.50

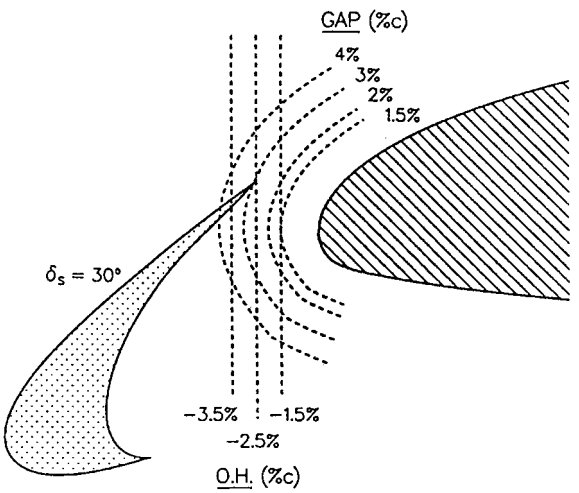

Slat rigging

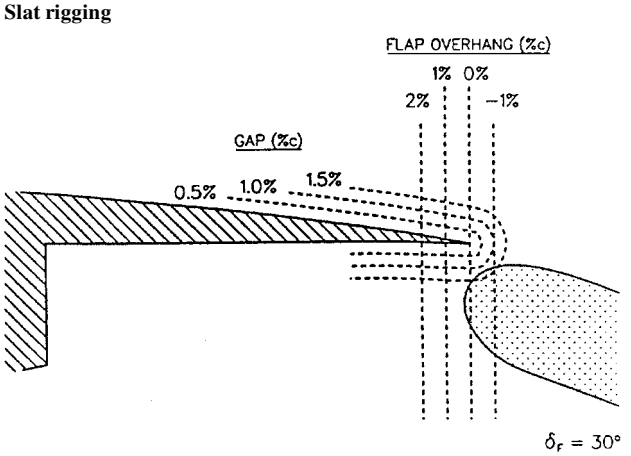

Flap rigging

Fig. 1 Definitions of gap and overhang for multielement airfoils.

Table 2 Flap gap, overhang (% of chord), and deflection, deg

Configuration	Gap	Overhang	Deflection
A, D	1.27	0.25	30
B	1.50	0.25	30
C	0.95	0.00	35

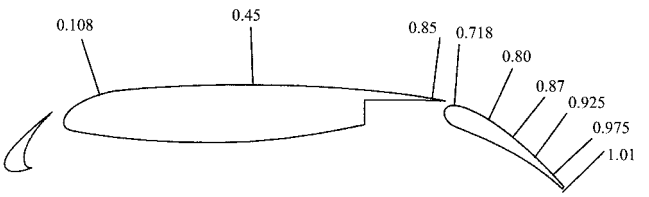

a) Configuration A with typical survey locations

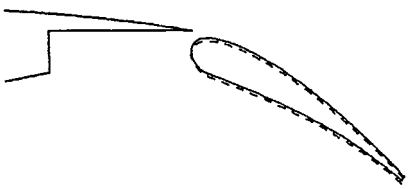

b) Configuration B

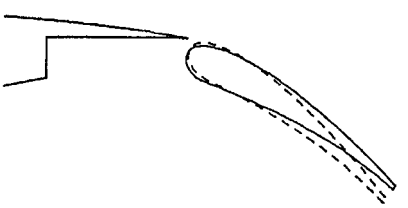

c) Configuration C

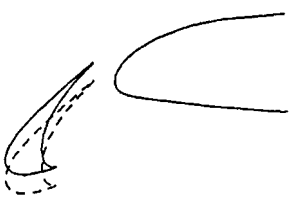

d) Configuration D

Fig. 2 Baseline multielement airfoil section and rigging variations; ——, configuration A, and – – –, alternate riggings.

Instrumentation and Test Procedure

Model pressures were measured by the LTPT PSI pressure measuring system consisting of electronic sensing pressure (ESP) modules. The ESP modules had differential pressure ranges varying from ±15 to ±100 psi with an accuracy of ±0.1% of their full-scale range. Pressure distributions obtained at 50% span were integrated to determine lift. Drag was calculated by integration of the static and total pressures obtained by the wake-rake system. Values of drag were computed for $\alpha \leq 16$ deg. Uncertainty estimates for the lift and drag data are based on both the observed test-to-test repeatability and influence of the traversing unit on these data. The overall uncertainty estimates for lift and drag coefficients are ±0.03 and ±0.001, respectively. Changes in lift associated with rigging changes during a single test can be resolved greater accuracy, approximately ±0.015. A discussion of repeatability and the

Table 3 Estimated overall uncertainties in five-hole probe measurements

θ, deg	$\delta\theta$, deg	θC_{pt}	θC_p
0	0.53	0.003	0.003
20	0.53	0.020	0.038
30	0.36	0.024	0.040

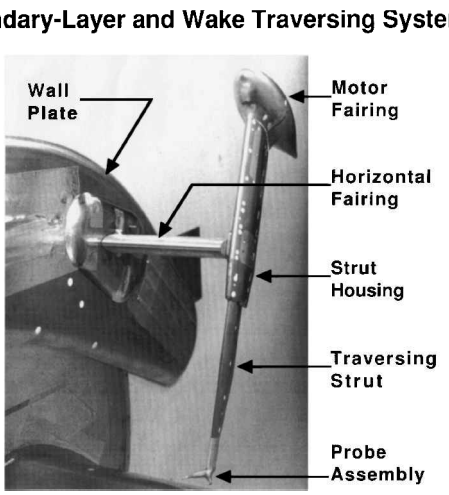

Fig. 3 Boundary-layer traversing system.

influence of the traversing unit on the airfoil flowfield is presented in Ref. 5.

The boundary-layer traversing unit is shown in Fig. 3. The traversing unit consists of a streamlined traverser that is attached to a curved wall plate by a horizontal support. The position of the traversing strut and probe assembly is controlled by a stepper motor and measured with the aid of an optical encoder. The motor, encoder, and gear assembly are located within the motor fairing. A motor-driven, airfoil-shaped fairing surrounds the horizontal support, which can be aligned with the local flow direction during a run. The traverser is manually positioned along the wall plate and can be rotated about the axis of the horizontal support. The horizontal support positions the traverser at the 77% span location.

The probe assembly consists of a flat-tube pitot probe and a hemispherical-shaped five-hole probe mounted at the ends of two prongs. Calibration of the five-hole probe allows local total pressure, static pressure, velocity, and flow angularity to be determined from the probe-pressure data. The probe was calibrated from -10 to $+45$ deg in the pitch plane and ± 20 deg in the yaw plane. An error analysis was performed on the five-hole probe calibration and data acquisition process. Estimated overall uncertainties in total pressure, static pressure, and flow angularity (pitch and yaw angle uncertainties are the same) for five-hole probe data obtained at a chord Reynolds number of 9×10^6 are presented in Table 3. Gaps in the profiles represent locations where the data lie outside the range of the probe calibration. Most of the flowfield data were obtained from the five-hole probe; the flat-tube probe was used to resolve the boundary-layer profile near the surface. The flat-tube probe thickness is 0.010 in., and the five-hole probe diameter is 0.127 in. Spanwise separation of the probe tips is 1.34 in. The flat-tube probe tip is electrically insulated from the traverser and is connected to a fouling circuit, which senses contact with the surface. The centers of the probe tips are displaced vertically by 0.07–0.10 in. (the position of the flat-tube probe was occasionally adjusted between runs), to allow clearance for the five-hole probe when the flat-tube probe tip is in contact with the surface.

The traverser motor and encoder are connected directly to an IBM-type personal computer. The traverser is controlled and the position is recorded by software running on that computer. Probe pressures are measured by precision pressure transducers connected to the LTPT MODCOMP data acquisition system and are acquired by the traverser-control computer from that system through a sequence of interrogations of the MODCOMP. During most of the runs comprising this test, 20 data samples were obtained.

Data Reduction

Skin friction was estimated from most of the velocity profiles obtained from the flat-tube probe by means of the Clauser chart technique.[6,11] Velocity profiles used to estimate C_f were computed from the flat-tube total-pressure data and the static pressure measured by the surface static-pressure orifice. The estimated uncertainty in the skin-friction coefficient data is ± 0.0005, based on observed repeatability and on comparison of the present data with results of Preston-tube measurements.[12]

Because of the relatively large values of unit Reynolds number corresponding to the present test conditions, the sublayer and the inner portion of the logarithmic region of the boundary layer are not resolved in these data. For this reason, some of the velocity-magnitude profiles do not appear to approach zero with decreasing distance from the surface.

The conventional definition of displacement thickness applies to a uniform external flow. With few exceptions, the viscous layers in the present series of experiments were embedded in regions of significant static-pressure variation normal to the local mean flow direction. The definition of δ^* used here is an attempt to remain as close as possible to the conventional definition. An inviscid velocity distribution is based on the freestream stagnation pressure and the smoothed static-pressure distribution. A corresponding density distribution is computed from the pressure and velocity distributions, using the assumption of constant stagnation temperature. The displacement thickness δ^* is defined in terms of an integral of the difference between the inviscid and measured profiles and reference conditions evaluated at the centroid of the mass flux deficit. At the stations downstream of the flap trailing edge, the integrals were terminated at the origin of the profile, the projection of the flap upper surface with the path of the traversing probe. This procedure excludes the contribution of the lower-surface boundary layer and provides integral properties that are consistent with profiles obtained farther upstream.

Regions of total-pressure deficit extend beyond the range of the probe traverse for a significant number of profiles obtained near the flap trailing edge. Integrals of these profiles, therefore, represent lower limits to accurate values. The accuracy of these profiles and the associated integrals is also limited by unsteadiness and three dimensionality. Examination of the profiles indicates that qualitative trends indicated by plots that include these data are correct. These data are indicated in the displacement-thickness plots (Fig. 15) by filled symbols.

Results and Discussion

Effect of Slat Position

Figure 4 shows a comparison of lift and drag data for configurations A and D. The slat for configuration D is translated downward relative to the A configuration, resulting in a reduced gap at a constant overhang and deflection angle. The general trends of increasing

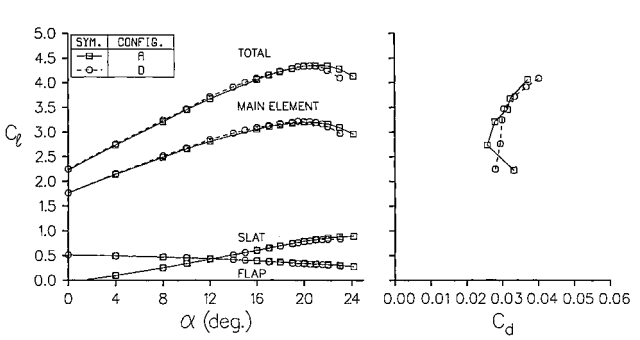

Fig. 4 Effect of change in slat position on lift and drag performance.

loading on the slat and main element and decreasing loading on the flap with increasing α are typical. The role of the wakes of upstream elements in decreasing the loading on the trailing-edge flap has been recognized for decades. The changes in aerodynamic characteristics caused by this change in slat position are small; the smaller slat gap is associated with a more pronounced loss in lift beyond stall and a small increase in drag at lower lift coefficient.

Static-pressure distributions for the three elements are compared in Fig. 5 for $\alpha = 21$ deg, that is, the maximum lift condition. The only differences between these two configurations are a slight increase of the suction peak on the main element associated with the closer proximity of the slat and more positive values of C_p on both surfaces of the slat near the trailing edge. This latter effect is associated with the slat trailing-edge position relative to the stagnation region on the main element.

Figure 6 presents velocity profiles obtained from the probe survey data for configurations A and D at the maximum lift condition, at the forward station on the main element, $x/c = 0.108$, and two stations on the flap, $x/c = 0.87$ and 0.925. Note the differences in both length and velocity scales between Fig. 6a (flow above the main element) and Figs. 6b and 6c (flow above the flap). The variations in velocity and length scales follow directly from the pressure distribution and the spreading of the wakes, respectively. Only the outer portion of the thin main-element boundary layer is resolved by the flat-tube probe at $x/c = 0.108$. Mixing of the slat wakes has reduced the minimum total-pressure deficits at $x/c = 0.108$, so that the velocity deficits in the slat wakes are small at this station. The shift in position of the slat wake remains evident in all of these profiles. The skin-friction measurements confirm that boundary-layer separation is not an issue on the main element over this angle-of-attack range.

It can be seen that, with this relatively small change in the slat gap, there is essentially no change in the boundary-layer portions of the profiles, in all but the outermost portion of the main-element wake. In other words, the slat gap has not been reduced to the point where it is having a significantly greater adverse effect on the wake spreading over the flap. This observation is consistent with the unchanged value of maximum lift. Note that $C_{l_{max}}$ is established when the rear portion of the main element is unloaded because of an unloading of the flap caused by the spreading wakes.

Detailed total-pressure data are presented in Fig. 7 for both slat positions at $x/c = 0.108$ and several angles of attack. Although the maximum values of velocity deficit in the wakes are small, the wake total-pressure profiles are adequately resolved at all angles of attack. The total-pressure profiles show a difference in character between the lower and the higher angles of attack. At the lower angles, up to 8 deg, the wakes are relatively wide and exhibit a small maximum total-pressure deficit. At $\alpha \geq 16$ deg, they become narrower, the centerline shifts farther from the surface, and the maximum values of total-pressure deficit become much larger. The two distinct types of slat wakes imply a qualitative change in the flow about the slat at $\alpha \approx 12$ deg. This change in character of the slat wake occurs in the same α range as the progression of transition from the trailing edge to the leading edge of the slat measured by Nakayama et al.,[13] and it seems clear that this progression of transition is the cause of the observed change in the slat wake profile.

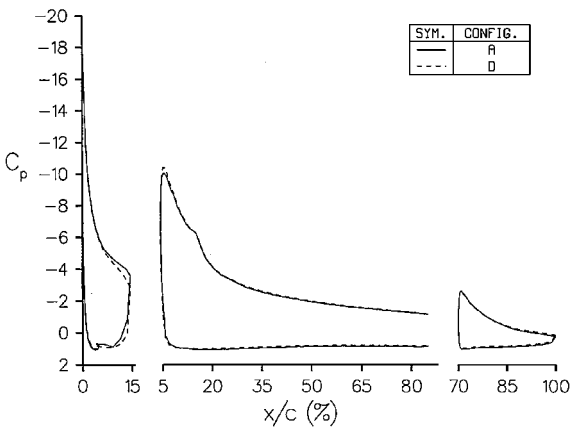

Fig. 5 Effect of change in slat position on static-pressure distributions, α = 21 deg.

Effect of Flap Position

Figure 8 shows a comparison of lift and drag data for configurations A and B. These results show how a small change in gap (0.23% increase from configuration A to configuration B) can cause a significant change in performance. Between $\alpha = 12$ and 16 deg, there is a reduction in lift and an increase in drag for configuration B relative to configuration A. However, beyond $\alpha = 16$ deg, the lift corresponding to configuration B is greater than that for configuration A. The $C_{l_{max}}$ for configuration B is approximately 0.05 greater than that for configuration A, and the stall angle is 1 deg greater. These results further illustrate how crucial the merging/spreading wakes are in establishing maximum lift characteristics.

Flap pressure distributions for both configurations are compared in Fig. 9 at $\alpha = 8$ and 16 deg. The flap suction peak is slightly higher for configuration B, which is consistent with the larger gap. At $\alpha = 8$ deg, the pressure is nearly constant over the aft portion of the flap upper surface for configuration B, indicating a tendency toward flow separation on the flap.

Comparisons of velocity profiles over the flap corresponding to the A and B configurations at $\alpha = 21$ deg are presented in Fig. 10. The profiles obtained near the flap leading edge, $x/c = 0.718$, show the high-velocity flow emanating from the gap between the main element and the flap. Note that these comparisons correspond to fixed locations with respect to the flap. The data associated with configuration B show a reduced tendency toward developing an off-body recirculation region above the flap and exhibit significantly less scatter in the profiles resulting from unsteadiness.

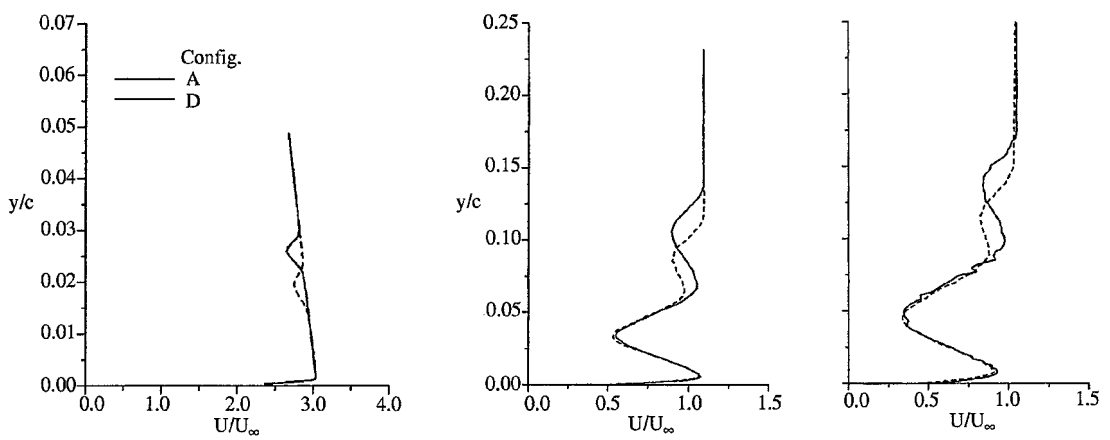

a) $x/c = 0.108$ b) $x/c = 0.87$ c) $x/c = 0.925$

Fig. 6 Effect of change in slat position on velocity profiles, α = 21 deg.

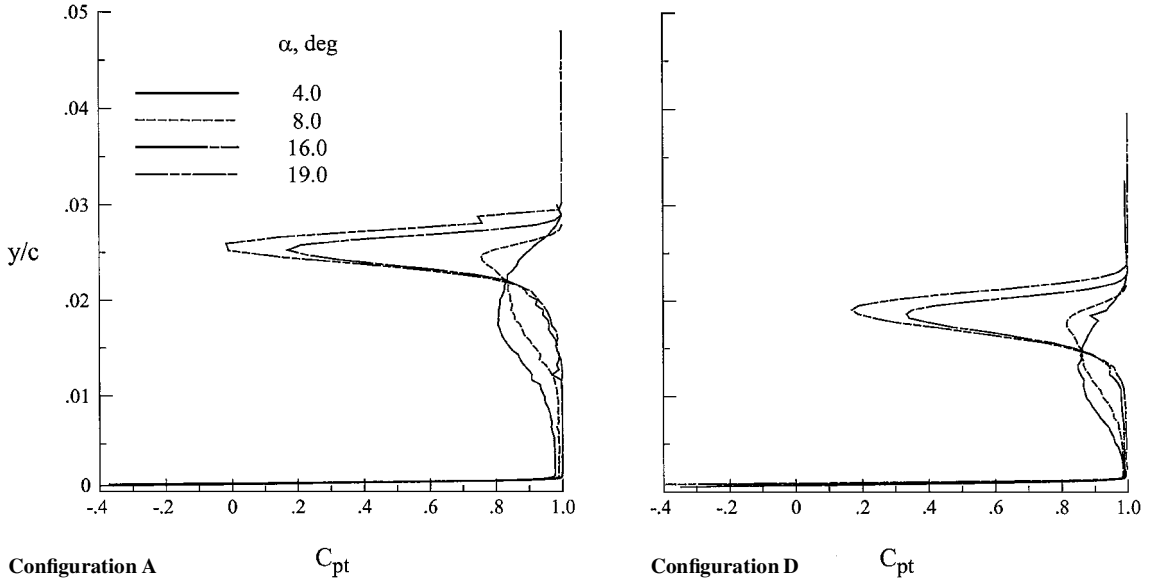

Fig. 7 Effect of angle of attack on total-pressure profiles, $x/c = 0.108$.

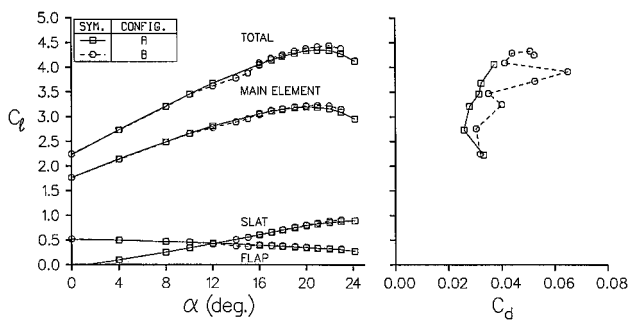

Fig. 8 Effect of increased flap gap on lift and drag performance.

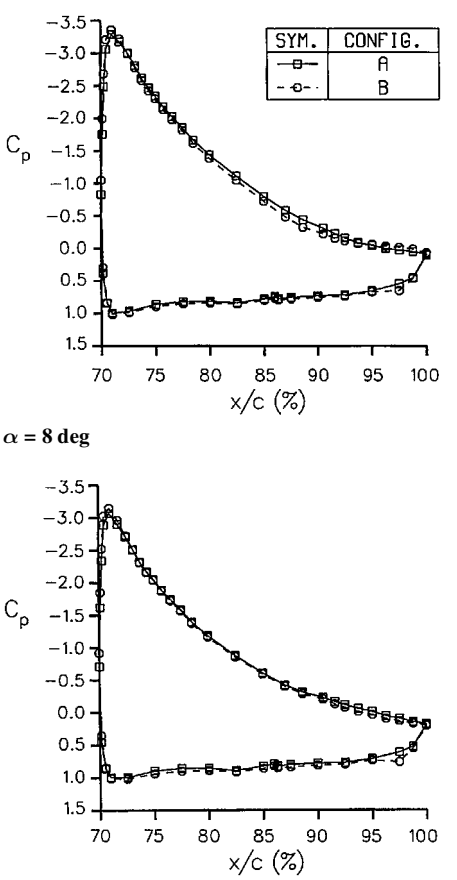

α = 8 deg

α = 16 deg

Fig. 9 Effect of increased flap gap on flap static-pressure distributions.

Effect of Flap Deflection

Lift and drag data for configurations A and C are compared in Fig. 11 (recall that the C configuration corresponds to a 5-deg increase in flap deflection relative to configuration A). It can be seen from Fig. 11 that the total lift at intermediate angles of attack was not increased with increasing flap deflection, thereby implying an offsetting flow separation on the flap, which is confirmed by the flap pressure distributions shown in Fig. 12 at $\alpha = 12$ deg. A small increase in maximum lift was observed with the increased flap deflection, but substantially less than expected. It will be shown subsequently that the less-than-expected increase in maximum lift is associated with a significant increase in displacement thickness of the viscous regions above the flap, caused by the increased adverse pressure gradient associated with the increased flap deflection. Values of C_d corresponding to the 35-deg flap deflection are greater at intermediate values of C_l. This increased drag is associated with separation on the flap.

Figure 12 presents comparisons for the flap pressure distributions for $\alpha = 12$ and 16 deg. As expected, the leading-edge suction peak is greater for the larger flap deflection. The upper-surface pressure distribution for configuration C shows nearly constant pressure on the aft portion of the flap and negative values of C_p at the trailing edge for $\alpha = 12$ deg. These features are consistent with the presence of separated flow on the aft upper surface of the flap. The flap pressure distributions obtained at $\alpha = 16$ deg are similar for the two configurations, with the exception of the leading-edge suction peak and a reduced static-pressure gradient on the aft upper surface for configuration C.

Comparisons showing the effect of the change in flap deflection on velocity profiles corresponding to four angles of attack are shown in Fig. 13. A key difference between the flowfields associated with configurations A and C is that, for the latter, the flow is separated on the aft upper surface of the flap at low to moderate angles of attack. At $\alpha = 8$ deg, the profiles corresponding to configuration A are attached and steady, but the profile corresponding to configuration C shows evidence of separation. At $\alpha = 12$ deg, the flow for configuration C is separated and unsteady over the aft portion of the flap. By contrast, all of the profiles shown for $\alpha = 16$ deg (Fig. 13c) are steady and attached. Note the tendency of the main-element wake to follow the flap at $\alpha = 8$ deg, and the lack of this tendency at $\alpha = 21$ deg. At

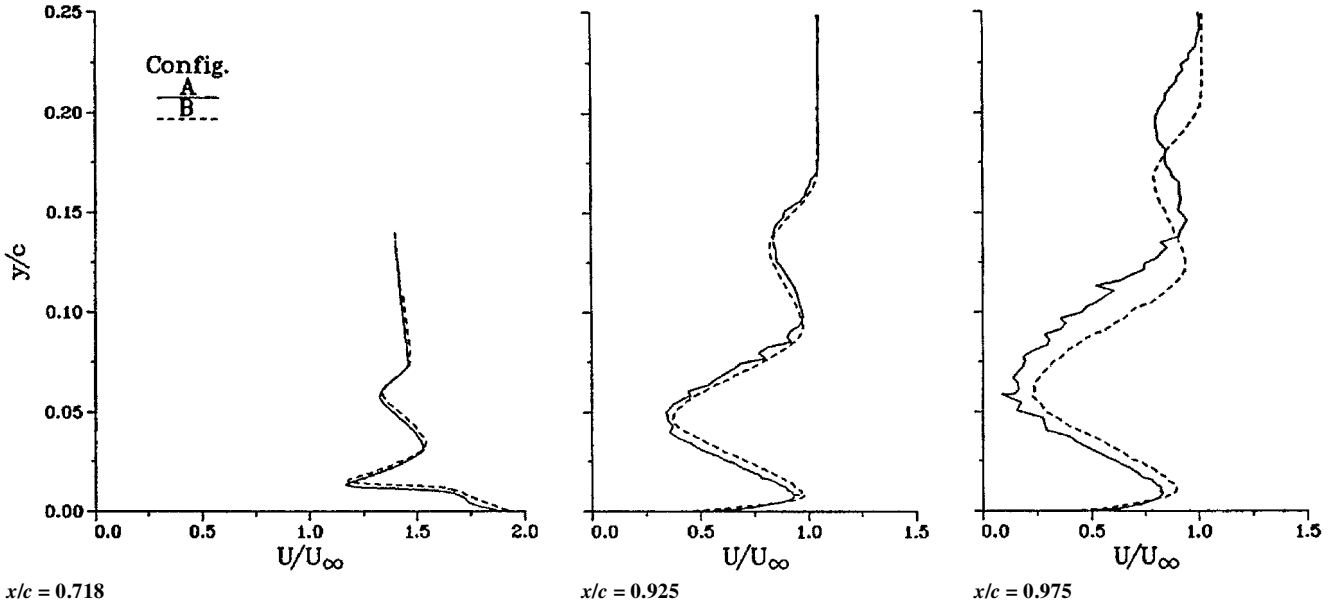

Fig. 10 Effect of increased flap gap on velocity profiles above the flap, α = 21 deg.

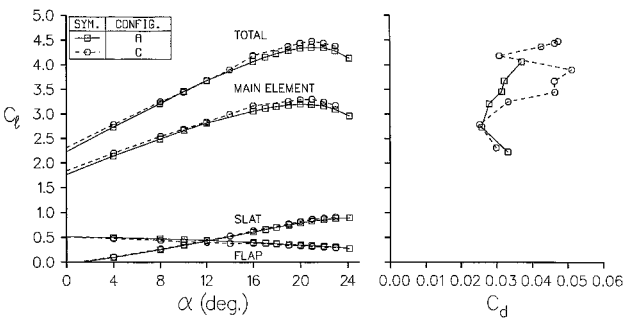

Fig. 11 Effect of increased flap deflection on lift and drag performance.

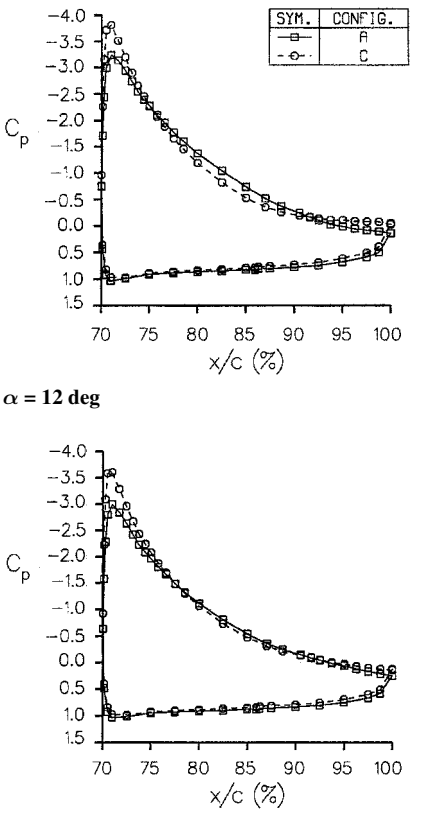

Fig. 12 Effect of flap deflection on flap static-pressure distributions.

angles of attack near $C_{l_{max}}$, the flap boundary layer is attached. As will be shown later, the increased flap deflection results primarily in an increase in the displacement thickness above the flap, rather than in the increased turning of the flow needed for an increase in lift. Wakes from the slat and the main element remain in approximately the same position in space as the flap deflection angle is increased.

Skin-Friction Data

Skin-friction data for configuration A obtained on the flap upper surface are compared successively with similar data corresponding to configurations B and C in Fig. 14. Variations with x/c and α are illustrated. Skin-friction coefficients presented in Figs. 14 are defined as the wall shear stress normalized by the freestream dynamic pressure. This type of comparison ensures that variations in skin-friction coefficient are associated with variations in wall shear stress, rather than from variations in local external-flow velocity or static pressure. The most forward station on the flap for which skin-friction data were obtained is x/c =0.80, which is forward of midchord. The boundary layers on the flap at x/c =0.718 were always too thin to permit skin friction to be estimated by the Clauser technique.

For configuration A, these data show 1) decreasing C_f with increasing x/c for all angles of attack and 2) decreasing C_f with increasing α at the forward station and increasing C_f with increasing α near the trailing edge. The latter trend is consistent with the decreased flap loading observed at the higher angles of attack. Skin-friction data corresponding to configuration B show consistently lower values at corresponding conditions than data obtained with configuration A. Several velocity profiles corresponding to configuration B at the lower values of α do not show a logarithmic region near the wall, an indication either of separation or incipient separation. Data corresponding to configuration C show significantly decreased values of skin friction relative to the baseline, with gaps in the data at the lower angles resulting from separation. Data obtained with configuration D (not shown) show values similar to the baseline data at the lower angles of attack and slightly lower values at the higher angles.

Following the present investigation, Preston-tube skin-friction measurements were made on this model by Klausmeyer and Lin.[12] In addition, a two-dimensional Reynolds-averaged Navier–Stokes code was used to compute the flow about this model for

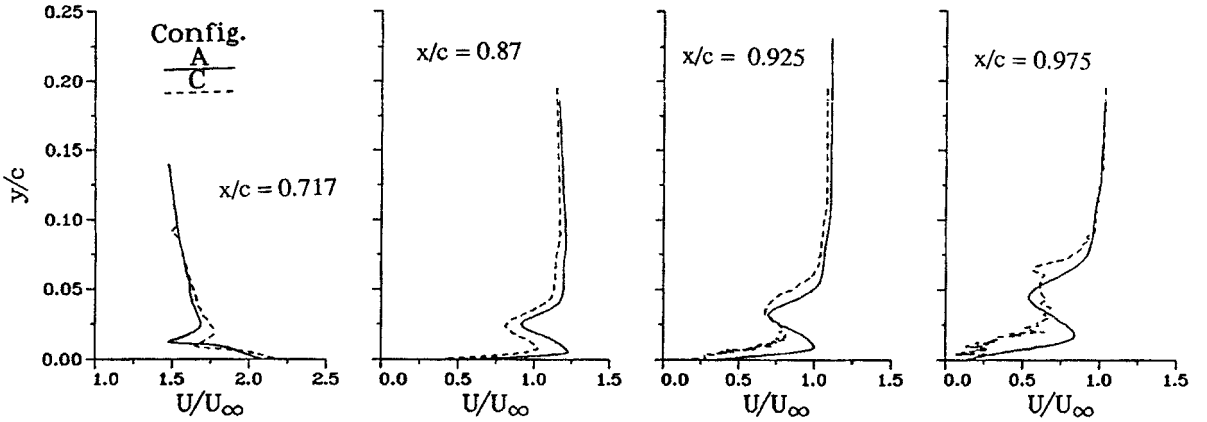

a) α = 8 deg

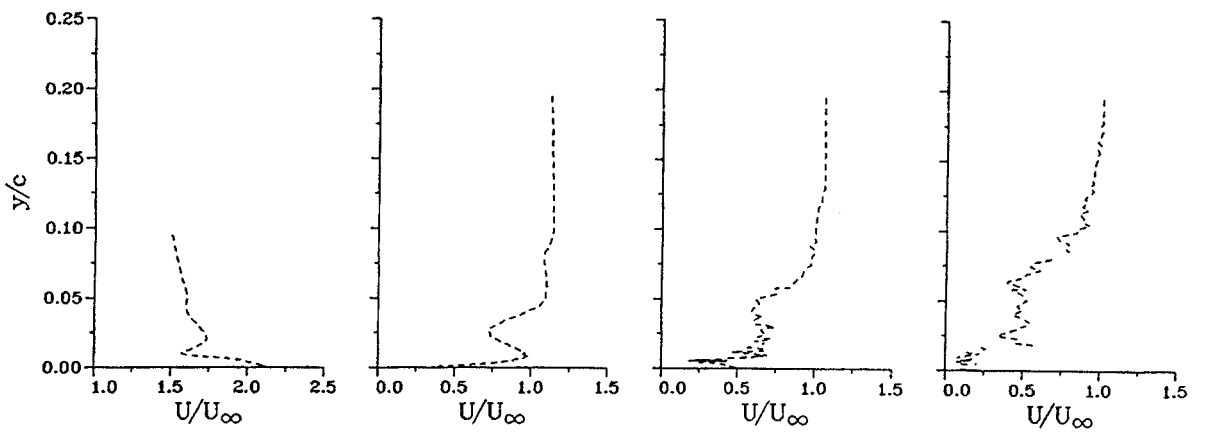

b) α = 12 deg

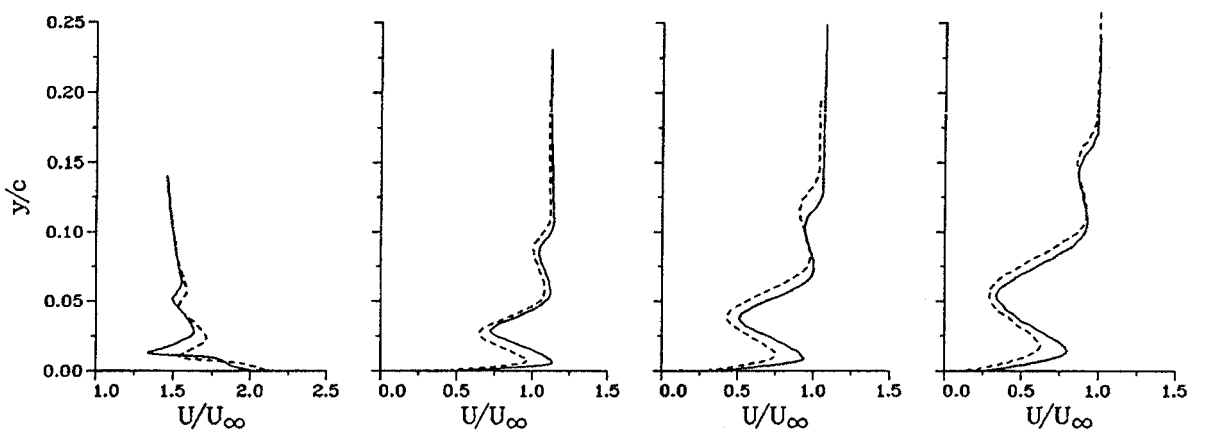

c) α = 16 deg

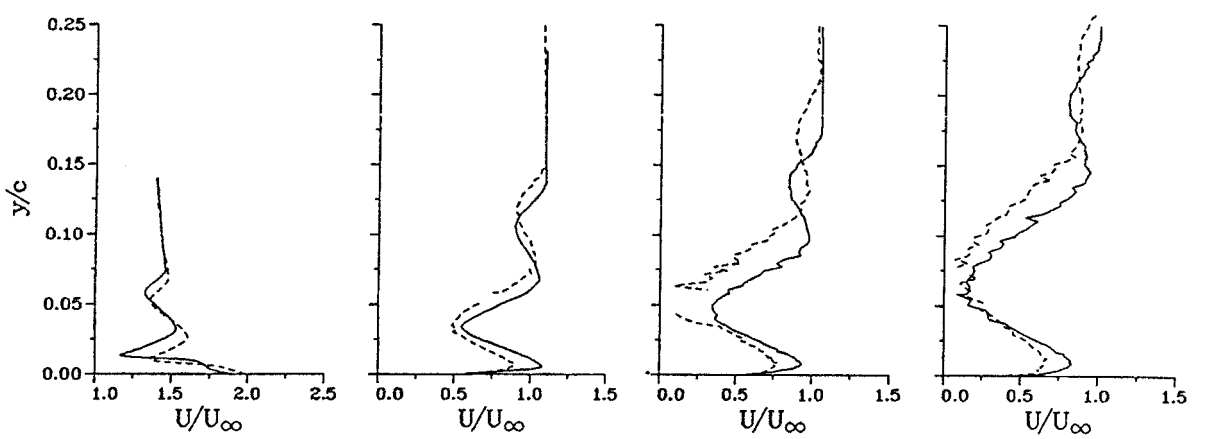

d) α = 21 deg

Fig. 13 Effect of increased flap deflection on velocity profiles above the flap.

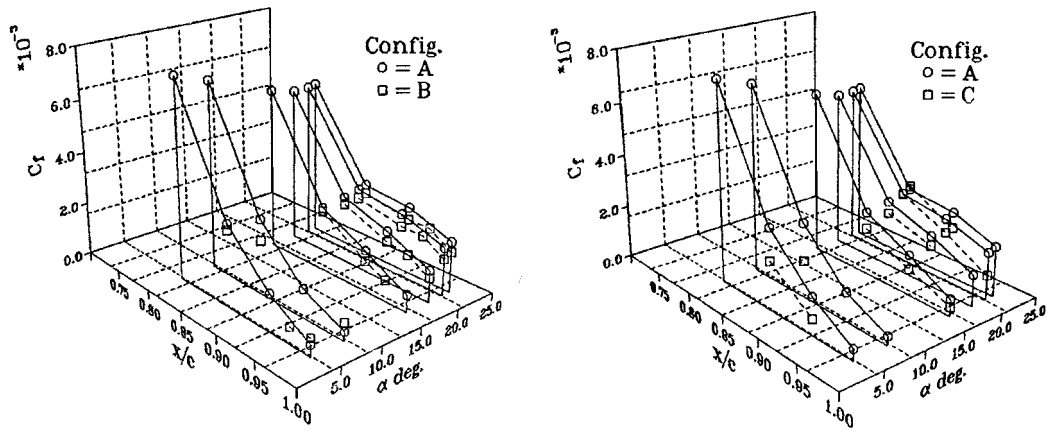

Fig. 14 Skin-friction distribution on the flap.

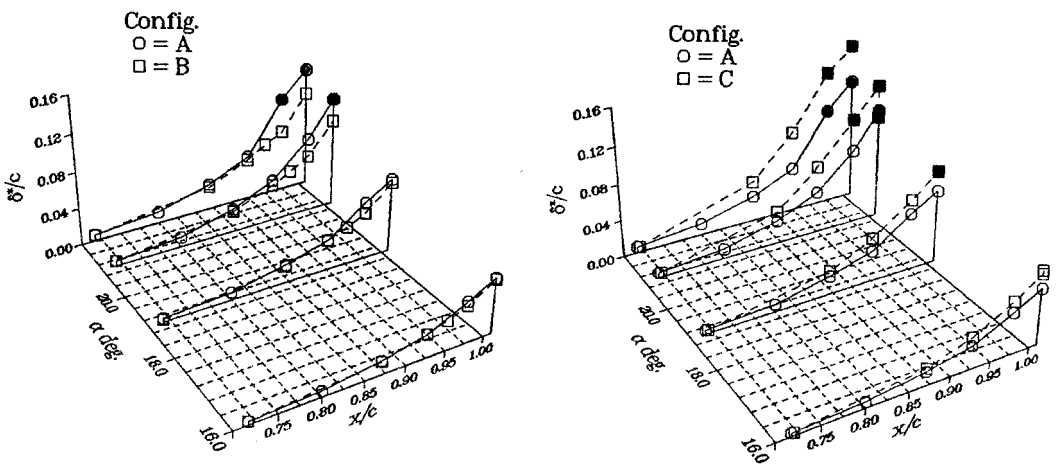

Fig. 15 Displacement-thickness distributions on the flap, filled symbols: wakes extend beyond range of probe traverse.

several test conditions. Data from the present investigation and both experimental and computed data from Ref. 12 were shown to be in good agreement.

Displacement-Thickness Data

Figure 15 presents distributions of displacement thickness above flap as a function of x/c and α. The data for configurations A and B are in good agreement at the lower angles of attack, including $\alpha = 4$ and 8 deg (not shown). At the higher angles, the values of δ^* are consistently smaller for configuration B. The data corresponding to configuration C show consistently larger values of δ^* than similar data obtained with configuration A. Also shown is a significant lack of repeatability for $\alpha = 21$ deg (approximately 30%) at the flap trailing edge for configuration C, associated with flow unsteadiness. The data corresponding to configurations A and D (not shown) are in good agreement at the lower angles of attack; at the higher angles and larger values of x/c, limited data show values of δ^* that are smaller for configuration D.

Conclusions

Data are presented from an experimental study of flow about an advanced multielement airfoil at high Reynolds numbers and lift coefficients extending beyond $C_{l_{max}}$. Data include surface static-pressure distributions, lift and drag measurements, and boundary-layer and wake surveys. The present study includes data corresponding to three perturbations in configuration geometry: a change in slat gap, a change in flap gap, and a change in flap deflection angle.

The results illustrate the following.

1) Spreading/merging wakes play a crucial role in establishing and controling the maximum lift capability of representative multielement high-lift airfoils. The maximum lift is caused the chain of events beginning with the rapidly spreading wakes above the flap that unload the flap. Unloading the flap, in turn, results in unloading the aft portion of the main element.

2) Interaction of the slat wake with the main-element boundary layer is negligible for representative slat riggings (slat gaps associated with good maximum-lift performance).

3) Flap riggings that promote merging of the flap boundary layer and main-element wake are associated with less-than-optimum maximum lift, but can be helpful in suppressing flap separation at approach angles of attack, thereby limiting improvements in maximum lift capability.

4) Subjecting the main-element and slat wakes to higher adverse pressure gradients by increasing flap deflection significantly increases wake spreading, thereby limiting any improvements in maximum lift capability with increasing flap deflection.

Data from this series of experiments are unique, in that they represent high Reynolds number flowfield measurements pertaining to stall of a multielement airfoil. The data are have been used for CFD code validation, and insights provided by these data should contribute to improved airfoil design.

Acknowledgment

This research was supported by the McDonnell Douglas Independent Research and Development Program and was performed in cooperation with NASA Langley Research Center.

References

[1] Valarezo, W. O., Dominik, C. J., McGhee, R. J., Goodman, W. L., and Paschal, K. B., "Multielement Airfoil Optimization for Maximum Lift at High Reynolds Number," AIAA Paper 91-13332, Sept. 1991.

[2]Lynch, F. T., "Experimental Necessities for Subsonic Transport Configuration Development," AIAA Paper 92-0158, Jan. 1992.

[3]Nakayama, A., Kreplin, H. P., Morgan, H. L., "Experimental Investigation of Flowfield About a Multielement Airfoil," *AIAA Journal*, Vol. 28, No. 1, 1990, pp. 14–21.

[4]Adair, D., and Horne, W. C., "Turbulent Separated Flow in the Vicinity of a Single-Slotted Airfoil Flap," AIAA Paper 88-0613, Jan. 1988.

[5]Chin, V. D., Peters, D. W., Spaid, F. W., and McGhee, R. J., "Flowfield Measurements About a Multi-Element Airfoil at High Reynolds Numbers," AIAA Paper 93-3137, July 1993.

[6]Spaid, F. W., and Lynch, F. T., "High Reynolds Number, Multi-Element Airfoil Flowfield Measurements," AIAA Paper 96-0682, Jan. 1996.

[7]Bertelrud, A., "Transition on a Three-Element High Lift Configuration at High Reynolds Numbers," AIAA Paper 98-0703, Jan. 1998.

[8]McGinley, C. B., Anders, J., and Spaid, F. W., "Measurements of Reynolds Stress Profiles on a High-Lift Airfoil," AIAA Paper 98-2620, June 1998.

[9]Lynch, F. T., Potter, R. C., and Spaid, F. W., "Requirements for Effective High-Lift CFD," International Council of the Aeronautical Sciences, Paper 96-2.7.1, Sept. 1996.

[10]Ying, S. X., Spaid, F. W., McGinley, C. B., and Rumsey, C. L., "Investigation of Confluent Boundary Layers in High-Lift Flows," AIAA Paper 98-2622, June 1998.

[11]Clauser, F. H., "Turbulent Boundary Layers in Adverse Pressure Gradients," *Journal of the Aeronautical Sciences*, Vol. 21, No. 2, 1954, pp. 91–108.

[12]Klausmeyer, S. M., and Lin, J. C., "An Experimental Investigation of Skin Friction on a Multi-Element Airfoil," AIAA Paper 94-1870, June 1994.

[13]Nakayama, A., Stack, J. P., Lin, J. C., and Valarzo, W. O., "Surface Hot-Film Technique for Measurements of Transition, Separation, and Reattachment Points," AIAA Paper 93-2918, July 1993.